COSMIC ORIGINS SPECTROGRAPH DETECTION OF Ne VIII TRACING WARM–HOT GAS TOWARD PKS 0405−123[*]

Anand Narayanan[1,2], Blair D. Savage[2], Bart P. Wakker[2], Charles W. Danforth[3], Yangsen Yao[3], Brian A. Keeney[3], J. Michael Shull[3], Kenneth R. Sembach[4], Cynthia S. Froning[3], and James C. Green[3]

[1] Indian Institute of Space Science & Technology, Thiruvananthapuram 695547, Kerala, India; anand@iist.ac.in
[2] Department of Astronomy, The University of Wisconsin-Madison, 5534 Sterling Hall, 475 North Charter Street, Madison, WI 53706-1582, USA;
savage@astro.wisc.edu; wakker@astro.wisc.edu
[3] Center for Astrophysics and Space Astronomy, Department of Astrophysical and Planetary Sciences, University of Colorado, 389 UCB, Boulder, CO 80309, USA
[4] Space Telescope Science Institute, 3700 San Martin Drive, Baltimore, MD 21218, USA

ABSTRACT

We report on the detection of Ne VIII in the *Hubble Space Telescope*/Cosmic Origins Spectrograph (COS) spectrum of the intervening absorption system at $z = 0.495096$ toward PKS 0405−123 ($z_{\rm em} = 0.5726$). The high signal-to-noise COS spectrum also covers absorption from H I, C III, O III, O IV, and O VI associated with this multiphase system. The Ne VIII is detected with high significance in both lines of the doublet, with integrated column densities of $\log N_a({\rm Ne\,VIII}\,770) = 13.96 \pm 0.06$ and $\log N_a({\rm Ne\,VIII}\,780) = 14.08 \pm 0.07$. We find the origin of Ne VIII consistent with collisionally ionized gas at $T \sim 5 \times 10^5$ K with a large baryonic column density of $N({\rm H}) \sim 10^{19}$–10^{20} cm^{-2}. The metallicity in the Ne VIII gas phase is estimated to be [Ne/H] $\sim -0.6 \pm 0.3$ dex. The intermediate ions such as C III, O III, O IV, and H I are consistent with photoionization in lower ionization gas at $T \sim 10^4$ K. The O V and O VI in this absorber can have contributions from both the photoionized and collisionally ionized gas phases. The absorber is at $|\Delta v| = 180$ km s^{-1} systematic velocity and $\rho = 110 h_{70}^{-1}$ kpc projected separation from an $M_R = -19.6$ galaxy of extended morphology. The collisionally ionized gas at $T \sim 5 \times 10^5$ K detected in Ne VIII and O VI points to an origin in multiphase gas embedded in the *hot* halo of the galaxy, or in a nearby WHIM structure. The high-sensitivity UV spectroscopy afforded by COS has opened up new opportunities for discovering large reservoirs of missing baryons in the low-z universe through the detection of Ne VIII systems.

Key words: galaxies: halos – intergalactic medium – quasars: absorption lines – quasars: individual (PKS 0405−123) – ultraviolet: general

Online-only material: color figures

1. INTRODUCTION

Absorption-line spectroscopy of distant quasars have yielded a complete census of the properties and distribution of baryons at the early epochs of the universe. At $z \gtrsim 3$, almost all of the baryons reside in the space in-between galaxies and galaxy clusters. This intergalactic medium (IGM) at high-z is almost entirely in the form of gas photoionized and heated to $T \sim 10^4$ K (e.g., Fukugita et al. 1998). The photoionized IGM manifests in the spectra of quasars as the Lyα forest. From those early epochs, the process of galaxy formation as well as the continued expansion of the universe is expected to have drastically altered the phase composition of much of the baryons (Cen & Ostriker 1999; Davé et al. 2001; Cen & Ostriker 2006). Observational efforts to detect these baryons in the present universe have so far not succeeded in identifying their most dominant reservoirs (Bregman 2007).

In the $z \sim 0$ universe, collapsed objects such as galaxies, groups, and clusters account for only $\lesssim 10\%$ of the cosmic baryon budget (Fukugita & Peebles 2004). More than 90% of the baryons are still outside of galaxies. However, unlike high-z, the fraction of intergalactic baryons in the photoionized phase

far from galaxies has significantly declined. Observationally, this is evident from the decline in the redshift distribution of Lyα absorbers (Kim et al. 1997; Weymann et al. 1998; Penton et al. 2000). Estimates suggest that in the present universe, the Lyα forest contribution to the baryon density ($\Omega_{\rm Ly\alpha}$) is only $\gtrsim 30\%$ (Penton et al. 2000, 2004; Lehner et al. 2007; Danforth & Shull 2008). This implies that a larger fraction of the intergalactic baryons must exist in a separate gas phase, not included in galaxies and also not dominantly photoionized. Numerical simulations of structure formation predict that most of these baryons are in highly ionized gas structures at temperatures in the range $T \sim 10^5$–10^7 K and densities of $n_{\rm H} \sim (0.1$–$10) \times 10^{-5}$ cm^{-3} (Cen & Ostriker 1999, 2006; Davé et al. 2001; Valageas et al. 2002). Frequently referred to as the Warm–Hot Intergalactic Medium (WHIM), this gas phase was an outcome of collisional ionization through heating in gravitational shocks when intergalactic matter fell into the potential wells of collapsed dark matter as structures grew hierarchically (e.g., Cen & Ostriker 1999). Detecting the WHIM and characterizing its physical properties remains one of the most important themes in observational cosmology. For extensive reviews on the search for WHIM in the low-z universe see Bregman (2007) and Prochaska & Tumlinson (2009).

UV absorption-line spectroscopy is presently the most promising approach for the detection and characterization of the WHIM. The diffuse nature predicted for the WHIM gas makes detection via emission scarcely possible. Also, attempts at observing the $T \gtrsim 10^6$ K WHIM in X-ray absorption at $z > 0$

have not been successful largely due to the insufficient sensitivity and resolution of the current generation of instruments. In the UV, the principal absorption-line tracers of collisionally ionized gas are O VI $\lambda\lambda$1032, 1038, Ne VIII $\lambda\lambda$770, 780, and broad Lyα (BLA). In gas in collisional ionization equilibrium (CIE), O VI reaches its peak ionization fraction at $T \sim 3 \times 10^5$ K. The strong O VI $\lambda\lambda$1032, 1038 doublet lines can thus be a sensitive probe of gas at those collisionally ionized temperatures (Tripp et al. 2000; Savage et al. 2002; Danforth & Shull 2008; Lehner et al. 2009; Narayanan et al. 2010a, 2010b). However, O VI is also produced in low density environments under the influence of a strong radiation field through pure photoionization at $T \sim 10^4$ K (Savage et al. 2002; Prochaska et al. 2004; Lehner et al. 2006; Thom & Chen 2008b; Tripp et al. 2008; Oppenheimer & Davé 2009). In the case of most O VI absorption systems, the complexity seen in absorption prevents a reliable assessment of the process that dominates the ionization.

In comparison, the Ne VIII $\lambda\lambda$770.409, 780.324 doublet lines ($f_{770} = 0.103$, $f_{780} = 0.0505$; Verner et al. 1994) are better tracers of collisionally ionized gas. Even though the cosmic abundance of neon is less compared to oxygen ((Ne/O)$_{\odot} = 0.17$; Asplund et al. 2009), detectable amounts of Ne VIII can be present in O VI absorbing gas at $T \sim (0.5$–$1.5) \times 10^6$ K. The temperature range corresponds to the *warm* phase of the WHIM. In CIE, the Ne VIII ionization fraction peaks at $T = 7 \times 10^5$ K. The first clear detection ($>3\sigma$) of Ne VIII doublet lines for an intervening absorber at low-z was reported by Savage et al. (2005), in the high signal-to-noise (S/N) *Far-Ultraviolet Spectroscopic Explorer* (*FUSE*) spectrum of the metal line system at $z = 0.20701$ toward HE 0226−4110. The column density of Ne VIII and its ratio with O VI were consistent with an origin in collisionally ionized gas at $T = 5.4 \times 10^5$ K with a substantial baryonic column of $N(H) \sim 8 \times 10^{19}$ cm^{-2}. The intermediate ions (such as C III, O III, O IV, Si III) and strong H I absorption in this system were created in a separate gas phase at $T \sim 2 \times 10^4$ K through photoionization. The second detection of Ne VIII was reported by Narayanan et al. (2009) in an intervening absorption-line system at $z = 0.32566$ in the *FUSE* spectrum of the quasar 3C 263. The redshifted wavelengths of O VI $\lambda\lambda$1032, 1038 lines in this absorber fell outside the wavelength coverage of *FUSE*. Nonetheless, the detection of ions such as O III, O IV, and N V in the *FUSE* spectrum pointed to the presence of both photoionized and collisionally ionized regions in the absorber, traced by the intermediate ions and Ne VIII, respectively. The detection of Ne VIII required the presence of gas with $T \gtrsim 10^5$ K, corresponding to the temperature anticipated for the *warm* phase of the WHIM.

Here, we report on another instance of Ne VIII detection in an intervening absorption system in the low-z universe. The Ne VIII $\lambda\lambda$770, 780 doublet lines are detected at high significance in the high S/N *Hubble Space Telescope*/Cosmic Origins Spectrograph (*HST*/COS) spectrum of the UV bright quasar PKS 0405−123. The detection distinctly points to the presence of *warm* collisionally ionized gas in a structure with a very large column density ($N(H) \gtrsim 10^{19}$ cm^{-2}) of baryons. This is the third in a series of COS detections of collisionally ionized gas in the regions surrounding galaxies, the other two being Savage et al. (2010) and Narayanan et al. (2010b).

2. OVERVIEW OF PREVIOUS WORK

The PKS 0405−123 sight line was previously observed by the *FUSE* and *HST*/STIS instruments at spectral resolutions of $\sim$20 km s^{-1} and $\sim$7 km s^{-1}. Lower resolution FOS observations

(FWHM $\sim$ 230 km s^{-1}) also exist for this target. A number of authors have published results on the detection and analysis of hydrogen and metal-line absorbers along this sight line (Bahcall et al. 1993; Jannuzi et al. 1998; Prochaska et al. 2004; Williger et al. 2006; Lehner et al. 2007; Tripp et al. 2008; Thom & Chen 2008a, 2008b; Howk et al. 2009). The most complete analysis of the ionization and chemical abundances in the $z = 0.495096$ absorber is given in Howk et al. (2009). A thorough investigation of the physical conditions was made possible by the combined *FUSE* and STIS coverage of several important low- and high-ionization metal species and hydrogen for this absorber.

In the *FUSE* spectrum, the Ne VIII $\lambda\lambda$770, 780 lines were non-detections with a 3σ upper limit on the equivalent width and column density of W_r(Ne VIII 770) < 29 mÅ and log N_a(Ne VIII) < 13.73 in the rest frame of the absorber (Howk et al. 2009). In the absence of Ne VIII, Howk et al. (2009) were able to determine a single-phase photoionization model that could simultaneously explain the column densities of all ions, including O VI. The constraints from the photoionization models, particularly the metallicity, were found to be dependent on the nature of the ionizing spectrum. In the best-fit models, an extragalactic ionizing background dictated by QSOs predicts carbon and oxygen abundances of −0.15 dex, whereas including the contribution of ionizing photons from star-forming galaxies, the abundances drop to −0.62 dex. The single-phase photoionization models derived by Howk et al. (2009) predict densities of $n_H \sim 5 \times 10^{-5}$ cm^{-3}, baryonic column densities of log $N(H) \sim 18.5$, a photoionization equilibrium temperature of $T \sim 28,000$ K, and a physical size of $L \sim 20$ kpc for the absorbing region. Howk et al. (2009) also do not rule out the possibility of the absorber having multiple gas phases, with at least one phase of predominantly photoionized gas ($T \sim 10^4$ K) and another warmer phase ($T \sim 10^5$ K) that is collisionally ionized. The absence of Ne VIII in the *FUSE* spectrum was accepted as evidence for the lack of $T \sim (0.5$–$3) \times 10^6$ K warm–hot gas associated with the absorber. The detection of Ne VIII in the higher sensitivity COS spectrum is a crucial new result, as it convincingly demonstrates that we are observing a substantial baryonic column of collisionally ionized gas, possibly the WHIM or the ionized halo of a galaxy.

3. COS OBSERVATIONS

The COS spectrum for PKS 0405−123 presented here is a combination of observations from the *HST* Early Release Program of 2009 August (Program ID: 11508) and GTO observations by the science team from 2009 December (Program ID: 11541). The details of the separate COS integrations are listed in Table 1. The exposures were retrieved from the *HST* archive and reduced in a uniform fashion using the most current CalCOS pipeline software (version 2.11). The reduced data were flux calibrated. The design capabilities of *HST*/COS are described in detail by Green (2001) and Froning & Green (2009) and in the updated COS Instrument Handbook (Dixon et al. 2010). The inflight performance of COS is discussed by Osterman et al. (2010) and in the numerous instrument science reports on the STScI COS Web site.[5] Savage et al. (2010) have used these COS observations of PKS 0405−123 to study the properties of the highly ionized plasma in the Lyman Limit system at $z = 0.1671$.

The separate G130M and G160M grating integrations were combined together in flux units weighted by their respective

---

Table 1
COS OBSERVATIONS OF PKS 0405−123

HST ID	Date of Observation (yyyy-mm-dd)	Grating	FP-POS	Central Wavelength (Å)	Wavelength Range (Å)	Exposure Duration (s)
LACB51010	2009-08-31	G130M	3	1291	1136–1430	984[a, b]
LACB51020	2009-08-31	G130M	3	1300	1147–1440	650
LACB51030	2009-08-31	G130M	3	1309	1156–1449	1908
LACB51040	2009-08-31	G130M	3	1300	1147–1440	650
LACB51050	2009-08-31	G130M	3	1318	1165–1459	1908
LACB51060	2009-08-31	G130M	3	1300	1147–1440	650
LACB51070	2009-08-31	G130M	3	1327	1175–1468	1908
LB6822010	2009-12-21	G160M	3	1589	1401–1761	2167
LB6822020	2009-12-21	G160M	3	1600	1412–1772	2965
LB6822030	2009-12-21	G160M	3	1611	1424–1784	2965
LB6822040	2009-12-21	G160M	3	1623	1436–1796	2965
LB6823010	2009-12-21	G130M	1	1291	1141–1435	1000[b]
	2009-12-21	G130M	2	1291	1138–1432	1400[a, b]
	2009-12-21	G130M	3	1291	1136–1430	1000[a, b]
	2009-12-21	G130M	4	1291	1133–1427	1430[a, b]

Notes. Column 1 is the *HST* ID for the respective data set, Column 2 shows the date of observation, Column 3 lists the choice of grating, Column 4 gives the FP position used with the grating setting, Column 5 shows the grating central wavelength setting, Column 6 gives the wavelength range covered under each setting, and Column 7 lists the duration of integration. *HST* IDs dated 2009-08-31 are *HST* Early Release Observations (ERO) with program ID: 11508, and those dated 2009-12-21 are GTO observations with program ID: 11541 (PI: James Green).
[a] The data sets used in the co-addition to produce the spectrum at the redshifted wavelength of Ne VIII λ770.
[b] The data sets used in the co-addition to produce the spectrum at the redshifted wavelength of Ne VIII λ780.

exposure time using the custom co-addition routine developed by Charles Danforth and the COS GTO team.[6] A full description of this routine is given in Danforth et al. (2010b). In brief, the routine cross-correlates and corrects the different exposures for velocity misalignments, before combining the fluxes. Since the FUV COS spectra are not flat-fielded, a procedure is built into the routine to psuedo-flat field each exposure to remove narrow fixed pattern features at the >10% depth (in flux units), most of which are repetitive grid-wire shadows. Applying this automated procedure does not result in the complete removal of every fixed pattern feature. Nonetheless, tests on several COS spectra have shown that the procedure is successful in removing periodic instrumental artifacts, thereby improving the overall sensitivity of the spectrum. The final co-added spectrum has wavelength coverage from 1135 Å to 1796 Å. The S/Ns (per 18 km s^{-1} resolution element) of this combined final spectrum at 1200 Å, 1400 Å, and 1600 Å are 20, 15, and 18, respectively. We also correct the COS spectrum for wavelength zero-point offsets. Weak low-ionization Milky Way ISM lines observed in the G130M and G160M integrations were used to check the reliability of the COS wavelength calibration. Based on the H I emission data given in Lockman & Savage (1995) we estimate the heliocentric velocity of the ISM absorption in the direction of PKS 0405−123 to be $v_{\mathrm{HELIO}} = 19.9$ km s^{-1}. To make the ISM lines in the PKS 0405−123 COS spectrum have average heliocentric velocities of 20 km s^{-1}, we applied velocity offsets of +6 km s^{-1} to the G130M and +22 km s^{-1} to the G160M data. Residual errors in the wavelength calibration correspond to ~5 km s^{-1}.

Ghavamian et al. (2009) have determined the resolving power of the spectrograph by detailed modeling of the line-spread function (LSF) at various wavelengths. The spectral resolution is found to be wavelength dependent with values in the range $\lambda/\Delta\lambda \sim 16{,}000$–21,000 for the G130M and G160M gratings, where $\Delta\lambda$ refers to the width at half strength of the LSF which has

broad wings containing ~20% of the LSF area. The resolution is maximum at near-UV wavelengths and declines monotonically toward lower wavelengths.

4. PROPERTIES OF THE Ne VIII SYSTEM

In this section, we describe the observed properties of the $z = 0.495096$ absorption system. In Figure 1, we display the continuum normalized absorption profiles in the rest frame of the absorber and in Table 1, we list the basic line measurements. For consistency, we adopt the same redshift for the system as given in Howk et al. (2009), which was based on the centroid of the C III λ977 profile from STIS. The COS spectrum for this system shows absorption from H I, O VI λλ1032, 1038, O IV λ788, C III λ977, O III λ833, and Ne VIII λλ770, 780. In addition, it also covers wavelengths where absorption from C II, N II, Si II, and Fe III are expected. For the line measurements, we use the apparent optical depth (AOD) method of Savage & Sembach (1991). For Lyβ, O VI, O IV, and C III we also apply Voigt profile models to estimate the column density, Doppler width and velocity associated with individual components. The fit models are shown in Figure 2. The profiles were fit with Voigt functions using the fitting routine of Fitzpatrick & Spitzer (1997). In this process, the model profiles were convolved with the COS instrumental spread function at the redshifted wavelength of the line. It is important that the specific LSF be used to fit the profile in order to minimize the impact of the LSF non-Gaussian wings on observed line profiles (see Ghavamian et al. 2009, for a detailed discussion). For completeness, we also show in Figure 1, the strong O V λ630 profile recorded at intermediate resolution by *FUSE* and the Lyα as seen by the low-resolution FOS. This is the first direct detection of O V in the IGM at low-z (Prochaska et al. 2004; Howk et al. 2009), and its absorption profile agrees well with the component structure for O VI seen in the COS data.

The O VI λλ1032, 1038 lines in the high S/N COS spectrum agree generally with the higher resolution, lower S/N observation from STIS. The O VI absorption is spread over
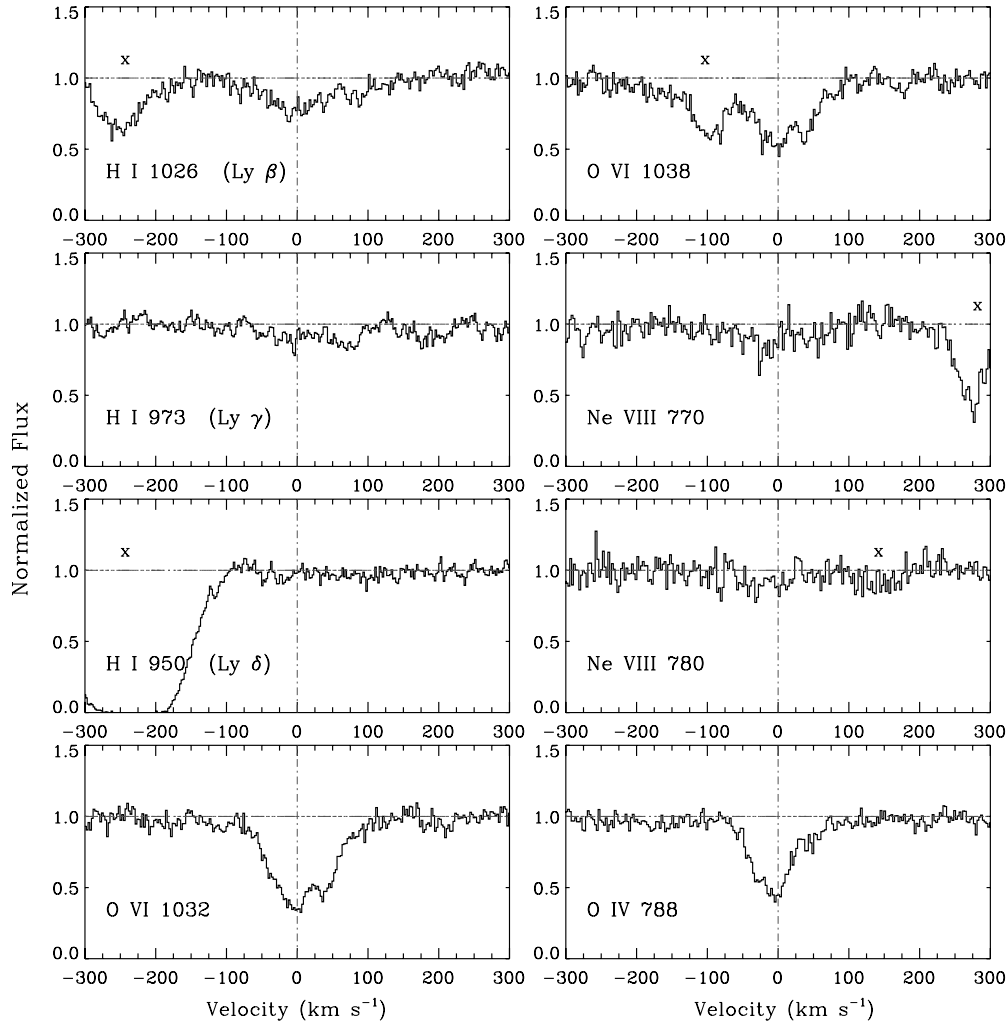
Figure 1. Continuum normalized spectrum of PKS 0405−123 showing absorption profiles and wavelength regions of some prominent lines in the $z = 0.495096$ metal line absorption system. The display is in the rest frame of the absorber, with $v = 0$ km s^{-1} corresponding to $z = 0.495096$. All panels are showing *HST*/COS spectrum, except O V λ630 and Lyα which are covered by *FUSE* and FOS observations, respectively. The individual exposures used to produce the co-added COS spectrum are listed in Table 1. Lyβ, O VI λλ1032, 1038, Ne VIII λλ770, 780, O IV λ788, C III λ977, and O III λ833 are COS detections of >3σ significance. Features that are not part of the absorption system are marked "x" in each panel. The line measurements are listed in Table 2.

$\Delta v \sim 250$ km s^{-1} and shows sub-component structure. In the STIS spectrum, a comparison of the apparent column density $N_a(v)$ profiles for the 1032 Å and 1038 Å lines had shown extra absorption in the 1038 Å line at $v \sim 30$ km s^{-1}, which was labeled as an unidentified interloping absorber (Howk et al. 2009). In the COS spectrum, we do not find any marked difference between the velocity components of the O VI doublet lines (see Figure 3). The contaminating feature in O VI 1038 Å, found in the STIS spectrum, is more likely a spectral artifact.

The $N_a(v)$ comparison of Figure 3 shows that the O VI lines are subjected to saturation that is unresolved by COS. The difference in the integrated apparent column densities of log $N_a(\text{O VI } 1032) = 14.39 \pm 0.01$, and log $N_a(\text{O VI } 1038) = 14.48 \pm 0.01$ is significant and suggestive of this unresolved saturation. The O VI 1038 column density measurement is within $\pm 1\sigma$ of the same by Howk et al. (2009) in the STIS spectrum and is likely to be a closer representation of the true column density. We correct for the line saturation effect using the procedure described in Savage & Sembach (1991) and obtain log $N_a(\text{O VI}) = 14.48 + 0.09 = 14.57$. The 0.09 dex saturation correction corresponds to the difference between the logarithmic column densities of the weaker (less saturated) and stronger

(more saturated) lines of the O VI doublet. The integrated O VI column density which we adopt in all subsequent analysis is the saturation corrected value of log $N_a(\text{O VI}) = 14.57 \pm 0.05$ dex.

The multiphase nature of the absorber becomes evident while comparing the apparent column density profiles across the absorption seen in the intermediate ions (C III, O IV) and the high ions (O V, O VI). The O IV and C III velocity structures resemble each other, as revealed by the arrangement of their $N_a(v)$ profiles displayed in Figure 3. The absorption from these ions over the -100 km s$^{-1} \leqslant v \leqslant 30$ km s^{-1} interval has a two component structure centered at velocities of $v \sim 0$ km s^{-1} and $v \sim -30$ km s^{-1}. However, the component at $v \sim -30$ km s^{-1} is not readily seen in O VI. It is likely that the slight asymmetry in the negative velocity portion of the O VI absorption is suggestive of an additional component, perhaps thermally broader than what is seen in O IV and C III. Additional evidence for the multiphase nature of the absorber is evident from the difference between the weak absorption seen in C III and O IV compared with the strong absorption in O VI over the velocity interval 30 km s$^{-1} \leqslant v \leqslant 80$ km s^{-1}. This indicates that the gas in this velocity range has higher ionization, compared to the gas at negative velocity, although they are likely kinematically linked
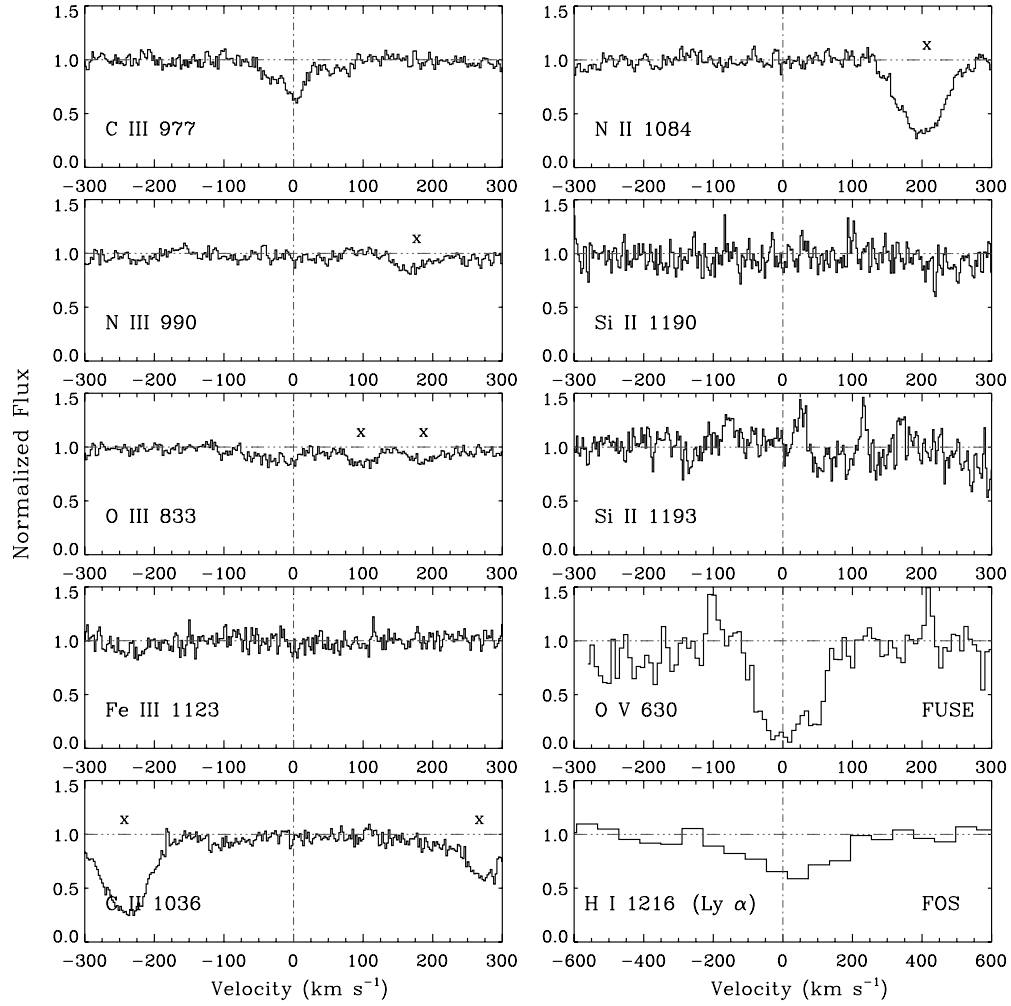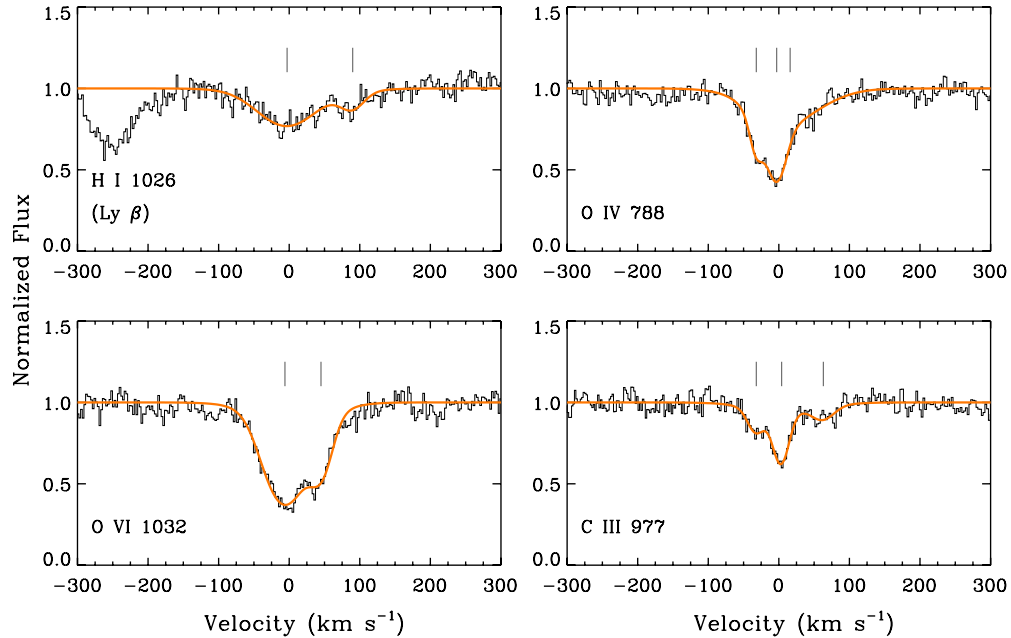
Figure 1. (Continued)

Figure 2. Voigt profile fit models superimposed on the $z = 0.495096$ Lyβ, O vi $\lambda1032$, O iv $\lambda788$, and C iii $\lambda977$ lines seen in the COS spectrum of PKS 0405−123. The profiles were fit using the Fitzpatrick & Spitzer (1997) routine. For each line, the model profiles were convolved with the COS instrumental spread function at the redshifted wavelength. The fit results are tabulated in Table 2. The centroid of the individual absorption components is marked by the vertical tick marks in each panel.

(A color version of this figure is available in the online journal.)
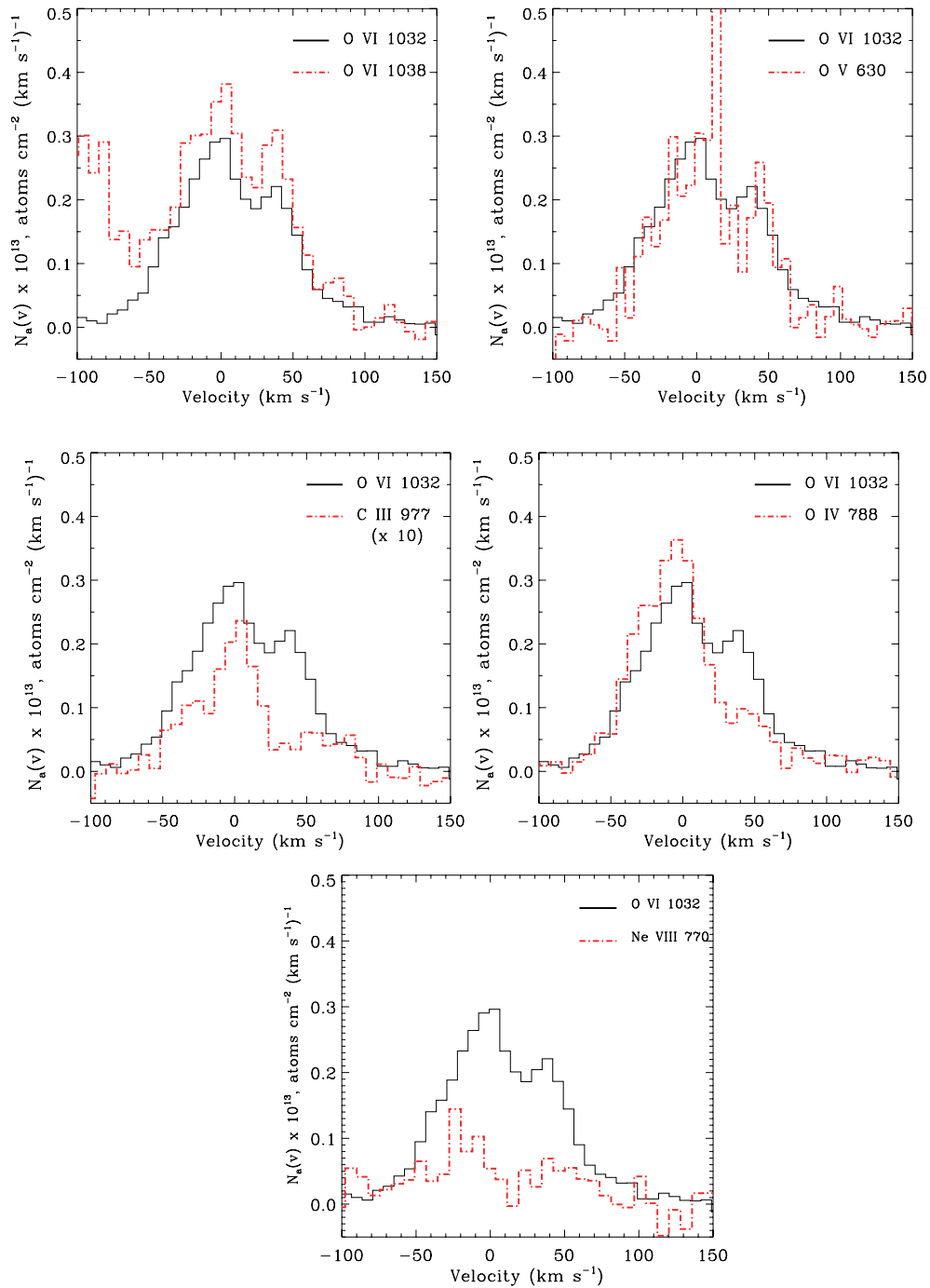
Figure 3. Apparent column density $N_a(v)$ profiles of the O VI $\lambda\lambda$1032, 1038 lines (top left panel), O V λ630 compared with O VI λ1032 (top right panel), O VI λ1032 compared with C III λ977 (middle left panel), and O VI λ1032 compared with O IV λ788 (middle right panel). The $N_a(v)$ profiles are displayed in the rest frame of the $z = 0.495096$ absorber. All profiles except O V are COS observations. The O V λ630 is from *FUSE*. The difference in the apparent column densities between the individual lines of the O VI doublet is indicative of unresolved saturation as discussed in Section 4. The O VI λ1038 is contaminated at $v < -50$ km s^{-1} by absorption unrelated to this system. The similarities between the component structures of O V and O VI is apparent and indicative of both ions predominantly tracing similar gas phase. The absorption in C III and O IV in the velocity interval $20 \leqslant v \leqslant 70$ km s^{-1} is weaker compared to O V and O VI. This could be due to higher ionization in the component of the gas producing the absorption. Apparent column density $N_a(v)$ profiles of the O VI λ1032 and Ne VIII λ770 lines (bottom panel). The $N_a(v)$ comparison reveals the similarity in component structure between Ne VIII and O VI, supporting the validity of the Ne VIII detection and also suggesting that the two ions could be tracing similar gas phases.

(A color version of this figure is available in the online journal.)

to each other. The integrated column densities for O IV and C III when compared to the STIS measurements suggest unresolved saturation for both lines. Howk et al. quote a lower limit of log N_a(O IV) $\gtrsim$ 14.37 and log N(C III) = 13.39 ± 0.05 adopted from component fitting. We adopt the same measurements for these two ions in our ionization analysis.

In the COS spectrum, O III λ833 is detected at $>3\sigma$ significance. The line is very weak and therefore was undetected at the sensitivity afforded by *FUSE*. The velocity range over which O III shows absorption concurs well with the velocity range of absorption from the higher ionization stages of oxygen. The rest-frame equivalent width W_r(O III 833) = 33 ± 2 mÅ and column

density log N_a(O III) $= 13.73 \pm 0.03$ that we measure from the COS data are consistent with the upper limits of $W_r < 36$ mÅ and log $N_a < 13.73$ obtained from *FUSE* by Howk et al. (2009). The errors on the O III equivalent width and column density do not include an estimated 5 mÅ and 0.06 dex systematic error produced by fixed pattern noise. With the detection of O III, we have column density measurements for four successive ionization stages of oxygen (O III–O VI), which sets useful constraints on the physical conditions in the absorber.

The information on H I associated with this absorber was poor in the existing STIS and FOS data. The FOS spectrum showed Lyα absorption at the redshift of the system, although the low resolution provided little information on the H I kinematics or the possibility of saturation. The Lyβ observed at higher resolution by *STIS* was poorly detected due to the low S/N ~ 6 pixel^{-1} of the recorded spectrum. The COS data offer a factor of three higher S/N coverage of Lyβ, along with tighter constraints on the H I column density from the higher order lines of the Lyman series. The Lyβ feature in COS is a clear but weak detection, with a central optical depth of $\tau_{\max}(v) \sim 0.3$. The H I is kinematically broad, spread over a velocity of $\Delta v \sim 350$ km s^{-1}. Based on simultaneous fits to the Lyα (FOS), Lyβ (STIS), and Lyγ (STIS, $<3\sigma$ significance) features, Howk et al. (2009) derive an H I column density of log N(H I) $= 14.29 \pm 0.10$. By integrating the $N_a(v)$ profile of Lyβ in the COS spectrum, we estimate the logarithmic total H I column density as 14.21 ± 0.02, consistent with the STIS measurement. At the COS resolution, the Lyβ appears to have two components, a broader principal component at $v \sim -3$ km s^{-1} blended with a $v \sim 90$ km s^{-1} component which could be narrower than the instrumental width. This positive velocity component is weaker and may not contribute significantly to the total H I column density. The profile fit to COS Lyβ yields b(H I) $= 53 \pm 1$ km s^{-1} for the principal $v \sim -3$ km s^{-1} component. If the broadening of this component is dominantly thermal, then the implied temperature is $T = 1.7 \times 10^5$ K. This component appears to be symmetric with respect to its centroid, although the COS instrumental resolution is not adequate to rule out of blending of closely separated components.

4.1. The Ne VIII $\lambda\lambda$770, 780 Detection

The wavelengths of the redshifted Ne VIII $\lambda\lambda$770, 780 lines are 1151.8 Å and 1166.2 Å, respectively. The Ne VIII λ770 line is therefore covered only by G130M grating observations at central wavelength settings of 1291 Å and 1300 Å. From the various COS integrations for this sight line, five exposures (with $t_{\exp} \geqslant 1000$ s) have central wavelength of $\lambda_c = 1291$ Å, and six shorter exposures ($t_{\exp} \sim 650$ s) have $\lambda_c = 1300$ Å. Similarly, the Ne VIII λ780 line is covered by G130M grating settings of central wavelengths 1291 Å, 1300 Å, 1309 Å, and 1318 Å.

The Ne VIII in this system is a relatively weak feature. To prevent gross systematic uncertainties from affecting the validity of the Ne VIII detection, we customized the combining of spectra in the wavelength range where absorption from the redshifted Ne VIII $\lambda\lambda$770, 780 lines were expected. We carefully chose for co-addition only those individual exposures for which we could clearly rule out grid-wire shadows or other detector artifacts (at the redshifted wavelengths of the Ne VIII doublet lines). Choosing different central wavelength grating settings allows the dispersed light to shift across the detector in the dispersion direction. For each setting, this enables the recording of the same wavelength by different regions of detector. By then aligning in detector space the different integrations, it becomes

possible to readily identify if the wavelengths corresponding to the Ne VIII $\lambda\lambda$770, 780 lines in each exposure are affected by any fixed pattern structure. In the case of PKS 0405−123, the individual integrations had adequate S/N to carry out this selection process with some certainty.

The spectrum at the wavelength of the Ne VIII λ770 line is co-addition of four G130M integrations at the $\lambda_c = 1291$ Å setting, resulting in a total exposure time of 5.8 ks at $\sim$1151.8 Å. The IDs of these four exposures are labeled in Table 1. At the Ne VIII λ780 Å redshifted wavelength, we found all five G130M integrations with $\lambda_c = 1291$ Å setting free of strong fixed pattern noise features and thus suitable for co-addition. These exposure IDs are also labeled in Table 1. The Ne VIII $\lambda\lambda$770, 780 lines displayed in the system plot of Figure 1 and the line measurements given in Table 2 are based on this revised co-addition.

By integrating over a 200 km s^{-1} velocity interval, we measure a rest-frame equivalent width of $W_r = 45 \pm 6$ mÅ for the Ne VIII λ770 line. The significance of the detection is 7.5σ. The 1σ uncertainty listed here includes both statistical errors and continuum placement error. A more conservative estimate of the detection significance should take into account systematic uncertainty from fixed pattern features that contribute to the noise at the $\sim$5 mÅ level. Including this systematic error, the Ne VIII λ770 is detected with a significance of 6.6σ.

At the location of the redshifted Ne VIII λ780 line, we also see absorption that is consistent with the 770 Å line. We measure a rest-equivalent width of W_r(Ne VIII 780) $= 29 \pm 5$ mÅ for this feature implying a detection significance of 5.8σ, excluding the systematic uncertainty from fixed pattern noise. The ratio W_r(Ne VIII 770)$/W_r$(Ne VIII 780) ~ 1.7 is close to the expected 2:1 line strength ratio for a doublet, further validating the Ne VIII detection. The integrated apparent column densities obtained for the two Ne VIII lines are also within 1σ of each other. In subsequent analysis, we use log $N_a = 13.96 \pm 0.06$ measured for the Ne VIII λ770 line as the Ne VIII column density in this absorber.

The rest-frame equivalent width we obtain for the Ne VIII λ770 of $W_r = 45 \pm 6$ mÅ is somewhat larger than the 3σ upper limit of $W_r < 29$ mÅ obtained from the lower S/N *FUSE* observations of Howk et al. (2009). We independently re-measured the *FUSE* observations integrating over ± 100 km s^{-1} and obtain $W_r = 38 \pm 12$ mÅ, which implies a 3σ detection. Our COS measurement is therefore in agreement with our new measurement of the *FUSE* spectrum. The validity of the COS detection of the Ne VIII λ770 line is further supported by the matching line profile observed for the much stronger O VI λ1032 line (see Figure 1(a)).

In Figure 3, we compare the apparent column density profiles of Ne VIII λ770 and O VI λ1032 lines. The $N_a(v)$ plot reveals the similarity in component structure between Ne VIII and O VI. In particular, the strong absorption in O VI over the velocity interval -70 km s$^{-1} \leqslant v \leqslant 25$ km s^{-1} is well matched by the absorption seen in the Ne VIII λ770 line. If the two ions are tracing similar gas phases, a similarity in their component structure is expected. The good velocity correspondence between the Ne VIII and O VI also lends support to the validity of the Ne VIII detection.

5. IONIZATION IN THE ABSORBER

Our primary goal is to understand the ionization mechanism responsible for the production of Ne VIII. Additionally, we investigate the extent to which other high ions such as O V

Table 2
PKS0405−123 $z = 0.495096$ O VI–Ne VIII ABSORBER

Line	W_r (mÅ)	v (km s^{-1})	log [N(cm^{-2})] (dex)	b (km s^{-1})	[$-v$, $+v$] (km s^{-1})	Method	Note
Lyα	493 ± 40	8 ± 5	14.03 ± 0.05	161 ± 13	[−240, 320]	AOD	1
Lyβ	108 ± 6	4 ± 2	14.21 ± 0.02	85 ± 5	[−150, 150]	AOD	
Lyβ	⋯	−3 ± 3	14.09 ± 0.03	53 ± 1		Fit	
	⋯	90 ± 4	13.44 ± 0.09	21 ± 2			
Lyγ	52 ± 4	14 ± 8	14.36 ± 0.04	93 ± 12	[−150, 150]	AOD	2
O VI 1032	223 ± 4	−1 ± 1	14.39 ± 0.01	54 ± 4	[−100, 150]	AOD	3
O VI 1032	222 ± 4	0 ± 2	14.39 ± 0.01	51 ± 3	[−100, 100]	AOD	
O VI 1032	⋯	−6 ± 2	14.29 ± 0.02	35 ± 1		Fit	
	⋯	45 ± 2	13.80 ± 0.07	19 ± 2			
O VI 1038	153 ± 5	−2 ± 4	14.48 ± 0.01	50 ± 4	[−70, 105]	AOD	3
Ne VIII 770	45 ± 6	−8 ± 5	13.96 ± 0.06	70 ± 4	[−100, 100]	AOD	4
Ne VIII 780	29 ± 5	−13 ± 11	14.08 ± 0.07	78 ± 7	[−100, 100]	AOD	5
O IV 788	108 ± 4	−9 ± 2	14.35 ± 0.01	52 ± 7	[−100, 150]	AOD	
O IV 788	⋯	−32 ± 3	13.73 ± 0.11	8 ± 2		Fit	
	⋯	−3 ± 2	14.09 ± 0.06	13 ± 1			
	⋯	16 ± 8	13.97 ± 0.08	62 ± 1			
O V 630	188 ± 18	12 ± 4	> 14.3	54 ± 8	[−100, 150]	AOD	6
C III 977	76 ± 5	−5 ± 2	13.13 ± 0.03	55 ± 7	[−100, 150]	AOD	
C III 977	⋯	−32 ± 3	12.52 ± 0.07	12 ± 2		Fit	
	⋯	4 ± 1	12.94 ± 0.03	11 ± 1			
	⋯	63 ± 3	12.40 ± 0.07	20 ± 1			
O III 833	33 ± 2	−26 ± 6	13.73 ± 0.03	53 ± 3	[−100, 55]	3σ	
C II 1036	<16	⋯	<13.2	⋯	[−100, 150]	3σ	
N III 990	<13	⋯	<13.1	⋯	[−100, 150]	3σ	
N II 1084	<54	⋯	<12.9	⋯	[−100, 150]	3σ	
O III 833	<49	⋯	<13.9	⋯	[−100, 150]	3σ	
Si II 1190	<42	⋯	<13.1	⋯	[−100, 150]	3σ	
Fe III 1123	<25	⋯	<13.5	⋯	[−100, 150]	3σ	

Notes. The listed errors on all the quantities only include the statistical errors. For W_r an additional ± 5 mÅ fixed pattern noise should be added to the statistical error for the COS observations. For v the COS calibration uncertainty of ∼ ± 5 km s^{-1} should be added to the listed statistical error. The errors listed for log N and b do not include the fixed pattern noise. The effect of fixed pattern noise will be small for large W_r and become important for $W_r < 40$ mÅ. (1) The Lyα measurement is from FOS. (2) The Lyγ component from 60 to 100 km s^{-1} is too strong to be consistent with the much weaker Lyβ absorption in that velocity range. With this apparent contamination, the Lyγ measurement should be treated with caution. (3) The different log N values for O VI $\lambda\lambda$1032, 1038 suggest significant line saturation for both lines. To a first approximation the true log N value is log N(O VI) = log N(O VI 1038) +Δlog N(O VI) = 14.48 ± 0.09 = 14.57 dex. The error on this value is ∼0.05 dex. (4) The Ne VIII λ770 observation is from a co-addition of one post-focus 1291 exposure and three GTO 1291 exposures. (5) The Ne VIII λ780 observation is from a co-addition of one post-focus 1291 exposure and four GTO 1291 exposures. (6) The O V λ630 measurement is from *FUSE* observations.

and O VI are produced in the gas phase traced by Ne VIII. We start the ionization discussion by considering the possibility of Ne VIII arising in a purely photoionized gas.

5.1. Is the Ne VIII Produced by Photoionization?

We use the photoionization code Cloudy (version C08.00; Ferland et al. 1998) to solve for time equilibrium models that reproduce N(Ne VIII). We treat the other ionic column densities as upper limits to account for the possibility that the absorber could have a mix of gas phases at different ionization levels. The source of ionization is assumed to be dominated by the extragalactic background radiation at the redshift of the absorber, whose shape and intensity are as modeled by Haardt & Madau (2001). The UV background which we use has contributions from quasars and young star-forming galaxies. The photoionization models are calculated for different ionization parameters[7] log U and metallicities, to select the model that best fits the observations. We assume that

the entire H I column density of 14.21 dex which we measure for this system is associated with the photoionized gas that we model. This assumption need not be valid for a multiphase absorber. Therefore, we comment on how lower N(H I) values in the Ne VIII gas would change the ionization predictions. In the models, we have assumed that the relative elemental abundance ratios are solar, with abundances of [C/H]$_\odot$ = −3.57 dex, [O/H]$_\odot$ = −3.31 dex, [Ne/H]$_\odot$ = −4.07 dex as given by Asplund et al. (2009).

In Figure 4, we display photoionization predicted ionic column densities for solar metallicity, log N(H I) = 14.21 and different log U. Recovering the observed Ne VIII column density through photoionization requires very high ionization parameter values. The observed log [N(Ne VIII)/N(O VI)] ∼ −0.6 is achieved at log U ∼ −0.2 (for solar abundance pattern), which corresponds to a number density of n_H ∼ 8 × 10^{-6} cm^{-3}, and a total hydrogen column density N(H) ∼ 6 × 10^{19} cm^{-2}. Such diffuse gas with large total hydrogen column density results in a large physical size of L ∼ 2.5 Mpc for the photoionized region. If the absorption is from an unvirialized structure, then the large path length would result in line broadening due

---

[7] Ionization parameter is defined as the ratio of the number density of photons with $E \geqslant 13.6$ eV to the total hydrogen density.
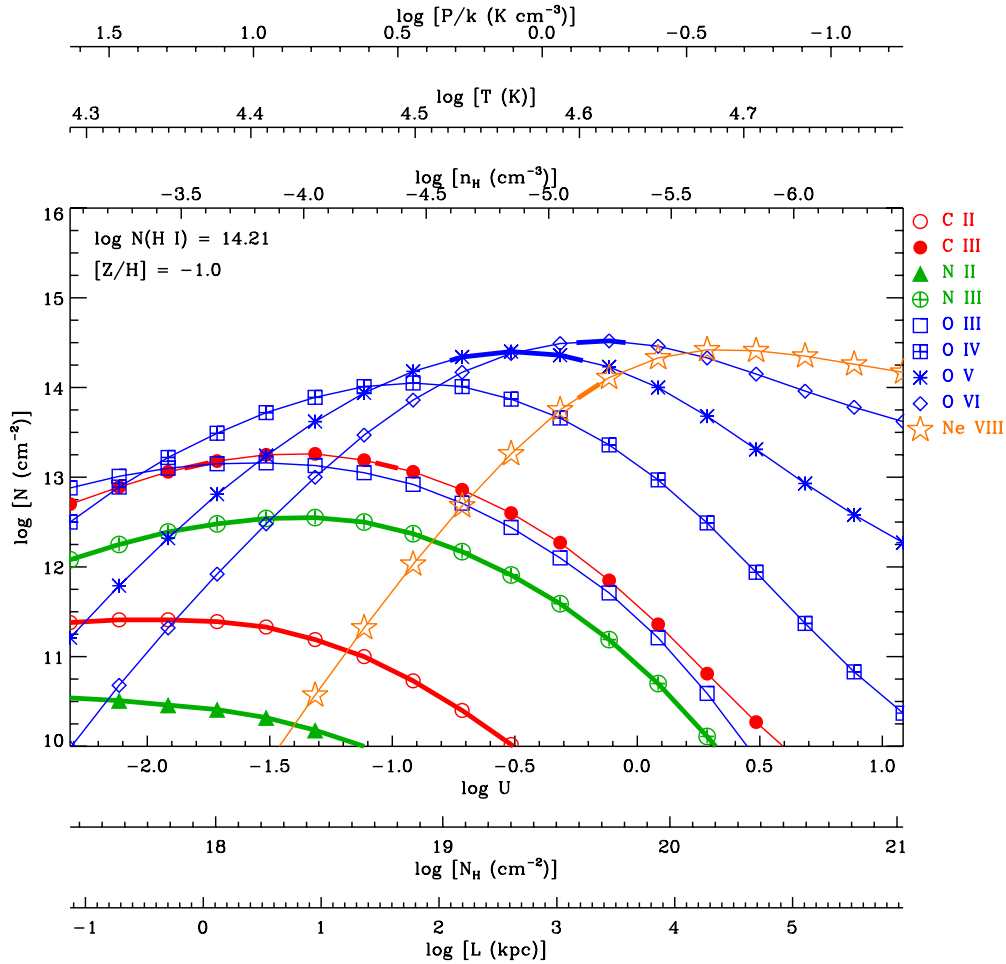
Figure 4. Photoionization (PI) equilibrium models computed using Cloudy for log $N(\text{H I}) = 14.21$ and 10% solar metallicity. We assume in these models the most recent solar relative elemental abundance estimations of Asplund et al. (2009). The different curves show the column density predictions made by the PI models at different ionization parameter (log U) values. The ionizing background is the Haardt & Madau (2001) model for $z = 0.495096$ which includes UV photons from quasars and young star-forming galaxies. The acceptable range of column densities for each ion, based on measurement, is highlighted in the photoionization curves using thick lines. The additional abscissa shows the predicted values for the number density (n_H), photoionization temperature (T), pressure (P/K), total hydrogen column density ($N(\text{H})$), and path length (L). The column densities of O VI and Ne VIII are simultaneously recovered for log $U = -0.2$. The physical conditions predicted by this model are discussed in Section 5.1.

(A color version of this figure is available in the online journal.)

to Hubble expansion of $v = H(z)L = 215$ km s^{-1}, much larger than the velocity width of the absorption seen in Ne VIII and O VI. If the observed O VI column also has contribution from the lower ionization gas phase traced by C III, O III, and O IV, then log $[N(\text{Ne VIII})/N(\text{O VI})] > -0.6$ implying log $U > -0.2$ and even lower densities leading to larger sizes for the absorber. The constraint on the ionization parameter is strongly dependent on the column density ratio between Ne VIII to O VI and does not vary significantly with metallicity or the H I column density. The unrealistic predictions of the models suggest that photoionization cannot be responsible for the production of Ne VIII in this absorber. The absorber can still have a photoionized phase where much of the H I and intermediate ion absorptions occur, as shown in Howk et al. (2009). Such multiphase nature can explain the clear differences in the component structure between the H I, C III, and O IV profiles with O V and O VI (see Figure 3).

If the absorber is residing in the halo of a galaxy, the local radiation field created by the galaxy could influence the ionization in the absorber (Fox et al. 2005). The ionization fractions of H I, and low ions such as C II, Si II, O III, and O IV can be influenced by the flux of UV photons escaping from

a star-forming galaxy. On the other hand, for the ionization fraction of O VI and Ne VIII to be altered, photons with energy $E \geqslant 113.9$ eV and $E \geqslant 207.3$ eV are required. O VI is produced at 113.9 eV and ionized at 138.1 eV. Similarly, Ne VIII is produced at 207.3 eV and ionized at 239.1 eV. The radiative intensities of O and B stars at such high energies are very low due to the significant opacity from He$^+$ ionization edge at $E \geqslant 54.4$ eV. Thus, the O VI and Ne VIII ionization levels are unlikely to be significantly altered by any local galactic radiation field.

5.2. Evidence for $T \sim 5 \times 10^5$ K Gas

5.2.1. Collisional Ionization Equilibrium

If CIE applies, the apparent column density ratio of log $[N_a(\text{Ne VIII})/N_a(\text{O VI})] = -0.61$ will be true for an equilibrium temperature of $T \sim 4.7 \times 10^5$ K (assuming solar abundances). If there is contribution from the photoionized phase to the total O VI column density, then the constraint would be log $[N(\text{Ne VIII})/N(\text{O VI})] > -0.61$, which is true for temperatures greater than 4.7×10^5 K. Thus, the presence of O VI provides a useful lower limit on the temperature of the gas producing
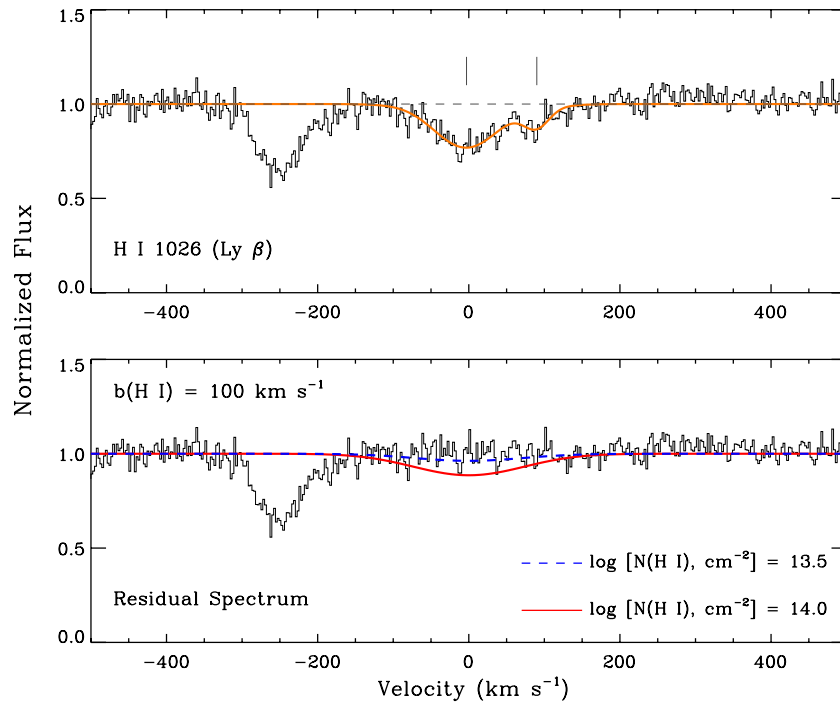
Figure 5. Top panel shows the $z = 0.495096$ rest-frame Lyβ absorption in the COS spectrum of PKS 0405−123. A Voigt profile fit to the H I absorption is shown as the thick line is overlaid on the spectrum. The bottom panel shows the residual absorption obtained after dividing the observed H I absorption with the fit model. Superimposed on this residual spectrum are synthetic Lyβ profiles with $b = 100$ km s^{-1} for two different H I column densities. The $b = 100$ km s^{-1} corresponds to the approximate thermal broadening to the H I line corresponding to $T \geqslant 4.7 \times 10^5$ K, the temperature predicted by CIE models for the gas producing the Ne VIII absorption. Based on the figure in the bottom panel we estimate the H I column in the collisionally ionized gas to be log N(H I) $\lesssim 13.5$.

(A color version of this figure is available in the online journal.)

the Ne VIII absorption. In gas at $T \geqslant 4.7 \times 10^5$ K, only a small fraction of the hydrogen would be in the neutral form ($f_{\rm HI} \lesssim N({\rm H\,I})/N({\rm H}) = 6.83 \times 10^{-7}$; Gnat & Sternberg 2007). Also, the H I absorption arising in such gas would be thermally broadened to $b({\rm H\,I}) \gtrsim 88$ km s^{-1}. This implies that much of the Lyβ absorption does not arise from the Ne VIII phase, but from lower ionization gas that is predominantly photoionized.

To derive the total hydrogen content of the absorber and the metallicity in the collisionally ionized gas, the H I column associated with this higher ionization Ne VIII phase has to be determined. However, the thermally broadened absorption from the trace neutral hydrogen associated with the Ne VIII gas would fall on top of the stronger absorption from the photoionized gas. It is therefore difficult to separate out this shallow and broad component of H I from the observed Lyβ profile. Therefore, one has to determine a column density upper limit for the broad H I indirectly. In Figure 5, we show the residual Lyβ absorption after dividing the Lyβ spectrum with the Voigt profile fit to feature. On top of this residual spectrum, we superimpose synthesized Lyβ profiles with $b({\rm H\,I}) = 100$ km s^{-1} and different column density values. It is evident from the figure that the broad H I associated with the Ne VIII gas has to be log N(H I) $\lesssim 13.5$ to be consistent with the data at the wavelength position of Lyβ. We use this adopted upper limit on H I column density to determine the metallicity and the baryonic content in the Ne VIII gas.

In Figure 6, we display Gnat & Sternberg (2007) CIE models for log N(H I) = 13.5. At $T = 4.7 \times 10^5$ K, the observed column densities of Ne VIII and O VI are well explained if we assume a metallicity of [Z/H] = −0.35. This CIE model would also account for $\lesssim$30% of the O V column, but little O IV or O III, consistent with their origin in a separate (photoionized)
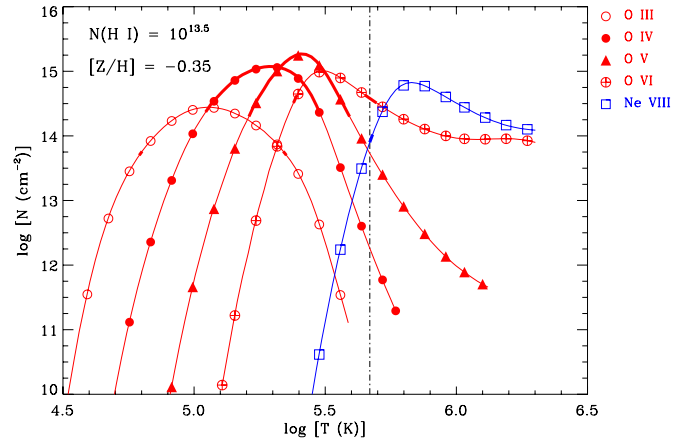
Figure 6. Column densities predicted by the CIE models of Gnat & Sternberg (2007) for Ne VIII, O VI, O V, O IV, and O III in the $z = 0.495096$ absorber, at the H I column density of 13.5 dex and −0.35 dex metallicity. We assume in these models solar relative elemental abundances given by Asplund et al. (2009) which includes the most recent updates for Ne and O. The regions on the respective CIE curves where the measured column densities are recovered (within ±1σ uncertainty) are highlighted using thick lines. The vertical dotted line marks $T = 4.7 \times 10^5$ K temperature at which the observed Ne VIII and O VI column densities are recovered simultaneously by a single-phase CIE model. This model can account for ~30% of the observed O V column density, but little O IV or O III suggesting an origin for those ions in a separate gas phase.

(A color version of this figure is available in the online journal.)

phase. The collisional ionization temperature and H I column density in the CIE model are lower and upper limits on the values they could assume. The observed Ne VIII column density can be reproduced even when log N(H I) < 13.5 by increasing the metallicity to values above −0.35 dex. The H I ionization

fraction at $T = 4.7 \times 10^5$ K implies that the Ne VIII gas is tracing a baryonic column of log $N(\mathrm{H}) \geqslant 19.67$. This lower limit on baryonic column density will be smaller for metallicities higher than -0.35 dex. It is worth noting that the metallicity inferred for the collisionally ionized gas is consistent with the metallicity range of $-0.62 \leqslant [Z/H] \leqslant -0.15$ estimated by Howk et al. (2009) for the photoionized gas phase of this absorber.

Gas that is heated to very high temperatures can undergo rapid radiative cooling at $T \sim 10^5$ K due to enhanced cooling efficiencies (Gnat & Sternberg 2007). Over time, the ion fractions in such gas would begin to show departures from CIE due to faster radiative cooling rate compared to the rate at which recombinations occur. However, for the temperatures that we infer for the Ne VIII gas, non-equilibrium ionization effects are minimal. At $T = 4.7 \times 10^5$ K, the Ne VIII and O VI fractions in a radiatively cooling gas at solar metallicity are $f_{\mathrm{Ne\,VIII}} = 5.26 \times 10^{-2}$ and $f_{\mathrm{O\,VI}} = 3.64 \times 10^{-2}$ (Gnat & Sternberg 2007). These values are only marginally different from the CIE values of $f_{\mathrm{Ne\,VIII}} = 4.87 \times 10^{-2}$ and $f_{\mathrm{O\,VI}} = 3.72 \times 10^{-2}$, and therefore yield similar predictions for the physical conditions.

5.2.2. Collisional and Photoionization Hybrid Models

The CIE analysis described in the previous section did not take into account the incidence of extragalactic ionizing radiation on the absorber. Even when conditions are conducive for collisional processes to dominate the ionization, a realistic modeling of absorption systems should also take into account the influence on ionization by the isotropic radiation field from quasars and star-forming galaxies (Danforth et al. 2006; Richter et al. 2006; Tripp et al. 2008; Danforth et al. 2010a; Narayanan et al. 2010b). We use Cloudy to compute simple *hybrid* models that allow both collisional and photoionization reactions to contribute toward the ionization in the Ne VIII gas phase. The temperature is fixed in Cloudy at $T = 4.7 \times 10^5$ K which is the lower limit on the temperature estimated from the CIE model for the Ne VIII gas phase. The model that Cloudy would converge on will have the ionization and recombination reactions in equilibrium, even though the heating and cooling rates will be out of balance due to the fixed temperature.

In Figure 7, we show a *hybrid* of photoionization and CIE model curves for the Ne VIII gas phase with log $N(\mathrm{H\,I}) = 13.5$, $T = 4.7 \times 10^5$ K and different log U values. Comparing the *hybrid* model column density predictions with the pure photoionization models displayed in Figure 4, we find that at log $U \lesssim -1.0$, the ionization fraction of both O VI and Ne VIII are higher (and almost a constant) due to the collision of electrons with ions contributing to the ionization at higher densities (smaller log U). The metallicity in this *hybrid* phase can have a range of values between $-0.9 \lesssim [Z/H] \lesssim -0.3$. From the shape of the $N(\mathrm{O\,VI})$ curve in Figure 7, it is evident that the upper limit of $[Z/H] \sim -0.3$ dex is based on the assumption that the O VI is exclusively produced in the *hybrid* phase. At this metallicity, $N(\mathrm{Ne\,VIII})$ and $N(\mathrm{O\,VI})$ are simultaneously recovered for log $U < -2.2$, which corresponds to a density of $n_H \gtrsim 8 \times 10^{-4}$ cm^{-3}, total hydrogen column density of $N(\mathrm{H}) \lesssim 5 \times 10^{19}$ cm^{-2}, and line-of-sight thickness of $L \lesssim 20$ kpc. For lower metallicities, log U has to increase in order to recover the measured $N(\mathrm{Ne\,VIII})$. The lower limit on the metallicity is the value at which Ne VIII is recovered near its peak in ionization fraction and at a log U that does not result in an excessively large path length for the absorbing region. In the *hybrid* model, those conditions are satisfied for $[Z/H] \sim -0.9$ and log $U \sim -0.5$ which corresponds to $n_H \sim 8 \times 10^{-6}$ cm^{-3},
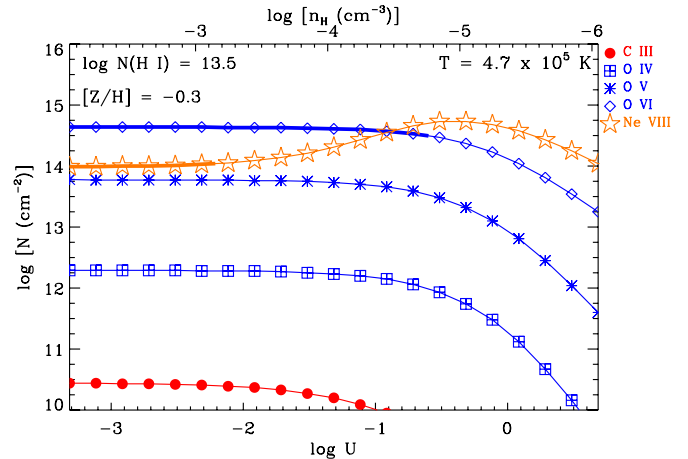
Figure 7. Column density predictions from CIE and photoionization *hybrid* models computed using Cloudy for the Ne VIII phase of the absorber. Solar relative elemental abundances given by Asplund et al. (2009) are assumed in these models. The temperature in the *hybrid* models is fixed at $T = 4.7 \times 10^5$ K given by the $N(\mathrm{Ne\,VIII})/N(\mathrm{O\,VI})$ at CIE (see Figure 6). The H I column density is determined from the Lyβ profile (see Section 5.2.1 and Figure 5). In the respective curves, the regions where the observed column densities are recovered (within $\pm 1\sigma$ uncertainty) are highlighted using thick lines. The column densities predicted for C II, N II, O III, and N III are less than 10^{10} cm^{-2} and hence are not displayed in the figure. The $[Z/H] = -0.3$ is the upper limit on metallicity. At that metallicity, for log $U < -2.2$, Ne VIII and O VI are simultaneously recovered from a single collisionally ionized phase. The physical conditions in the Ne VIII gas based on these *hybrid* models are discussed in Section 5.2.2.

(A color version of this figure is available in the online journal.)

$N(\mathrm{H}) \sim 10^{20}$ cm^{-2}, and $L \sim 4$ Mpc. Such a *hybrid* model would require the O VI to have significant contribution from the separate photoionized phase traced by the low and intermediate ions. To summarize, within the framework of these simple CIE and photoionization *hybrid* models, the Ne VIII gas phase has a metallicity of $[Z/H] = -0.6 \pm 0.3$ and log $U \lesssim -0.5$, which implies $n_H \lesssim 10^{-5}$ cm^{-3} and $N(\mathrm{H}) \sim 10^{19}$–$10^{20}$ cm^{-2}. The Ne VIII is produced via collisional ionization, whereas the O VI can have contribution from a separate gas phase that is predominantly photoionized.

6. GALAXIES IN THE VICINITY OF THE ABSORBER

Given the evidence for the presence of $T \sim 5 \times 10^5$ K gas, the location of the absorber with reference to galaxies becomes important. The absence of an optical counterpart to the absorber would strengthen the case for the absorption arising in an unvirialized WHIM structure in the IGM. Chen & Mulchaey (2009) have carried out imaging and spectroscopic search for galaxies in the PKS 0405$-$123 field. Their survey has a $>60\%$ completeness for galaxies brighter than $R = 22$ out to a separation of 2 arcmin from the line of sight, which corresponds to a projected distance of $\sim 734 h_{70}^{-1}$ kpc at $z = 0.4950$, assuming $\Omega_m = 0.28$ and $\Omega_\Lambda = 0.72$ (Wright 2006). The survey was 100% complete for galaxies brighter than $R = 20$. In this survey, a galaxy with rest-frame R magnitude of $M_R - 5 \log h_{70} = -19.6$ is identified close to the Ne VIII absorber at a projected distance of $\rho = 110 h_{70}^{-1}$ kpc. The galaxy's spectroscopic redshift is $z = 0.4942$, and thus is at a systemic velocity of $\Delta v = -180$ km s^{-1} with respect to the Ne VIII absorber. No other galaxy brighter than $R = 20$ is identified within a comoving distance of $3.7\, h_{70}^{-1}$ Mpc of the absorber. At this redshift, $M_R = -19.6$ corresponds to a galaxy luminosity of $0.08 L_R^*$ (Dahlen et al. 2005).

The galaxy displays an extended morphology in the high spatial resolution *HST*/WFPC2 image of the field (see Figure 10 of Chen & Mulchaey 2009). The galaxy's spectrum is dominated by strong emission lines from [O II], [O III], Lyγ, and Lyβ indicating activity in the underlying stellar population. The proximity of the Ne VIII absorber to the galaxy is an important, though not conclusive, indicator of the absorption possibly arising in the extended *hot* halo of the galaxy. In the case of the $z = 0.20701$ Ne VIII system toward HE 0226−4110 reported by Savage et al. (2005), three sub-L^* galaxies were identified within $\rho = 200$ kpc and $\Delta v = 300$ km s^{-1} of the absorber (Mulchaey & Chen 2009). Both these Ne VIII detections also show strong O VI absorption ($W_r > 30$ mÅ). It is known from a number of absorber-galaxy studies that O VI systems preferentially arise within the $\rho \lesssim 500$ kpc environment of $L*$ galaxies and even closer to $0.1L^*$ galaxies (Sembach et al. 2004; Tumlinson et al. 2005; Stocke et al. 2006; Tripp et al. 2006; Lehner et al. 2009; Wakker & Savage 2009; Chen & Mulchaey 2009). If Ne VIII is always associated with strong O VI systems, then they are also likely to be tracing collisionally ionized gas in circumgalactic environments. Investigating this correlation requires a large sample of Ne VIII detections.

The $[Z/H] \sim -0.6$ dex metallicity derived from the *hybrid* model for this Ne VIII absorber is more consistent with a halo origin rather than in the canonical WHIM structure tracing pristine IGM distant from galaxies, in which case lower metallicities are expected (Danforth et al. 2006). It is however important to bear in mind that the regions where galaxies interface with the IGM are complex environments influenced by a variety of inflow and outflow processes transferring matter and energy between the two systems. This blurs the distinction between what can be characterized as the halo or the IGM. It is difficult to be conclusive about the astrophysical origin of an absorption system based solely on one-dimensional information obtained by probing a pencil beam through such a complex environment.

6.1. Summary

We have reported on the detection of Ne VIII $\lambda\lambda$770, 780 lines in the intervening absorption system at $z = 0.495096$ in the COS high S/N spectrum of the quasar PKS 0405−123. This is the third clear detection of this ion in the low-z IGM. The significant results are summarized as follows.

1. Both members of the Ne VIII doublet in the $z = 0.495096$ multiphase absorber are detected at high significance (above the 5σ level) in the COS spectrum. The Ne VIII 770 line has a rest-frame equivalent width of $W_r = 45 \pm 6$ mÅ and an apparent column density of log $N_a = 13.96 \pm 0.06$, and the Ne VIII λ780 line has $W_r = 29 \pm 5$ mÅ and log $N_a = 14.08 \pm 0.07$. The Ne VIII absorption extends over the same velocity interval as the strong absorption from O VI $\lambda\lambda$1032, 1038 lines.

2. Also seen in the COS spectrum are Lyβ, C III, O III, O IV, and O VI associated with the absorber. The O III line was a non-detection at the 3σ significance level in the *FUSE* spectrum for this target. We measure W_r(O III 833) $= 33 \pm 2$ mÅ and log N_a(O III) $= 13.73 \pm 0.03$. The Lyβ absorption was poorly detected in the low S/N STIS spectrum. The higher sensitivity spectrum for Lyβ afforded by COS reveals subcomponent structure in H I, with an integrated apparent H I column density of log N_a(H I) $= 14.21 \pm 0.02$.

3. The column density of Ne VIII cannot be explained by gas that is purely photoionized by the extragalactic ionizing background radiation field. The detection of Ne VIII requires collisionally ionized gas with $T \sim 5 \times 10^5$ K. Gas at this temperature is highly ionized with a trace neutral H I fraction of $f_{H I} = N(H I)/N(H) \sim 7 \times 10^{-7}$. From the Ly$\beta$ profile, we estimate the H I column in this *warm* collisional phase to be log $N(H I) \lesssim 13.5$, which suggests that the Ne VIII is tracing a gas structure with a total hydrogen column density of $N(H) \sim 5 \times 10^{19}$ cm^{-2}.

4. *Hybrid* models that simultaneously take into account both collisional ionization and photoionization reactions predict a metallicity of $[Z/H] = -0.6 \pm 0.3$ dex in the Ne VIII gas phase. The density in this gas phase is constrained to $n_H \lesssim 10^{-5}$ cm^{-3} and total hydrogen column density to $N(H) \sim 10^{19}$–10^{20} cm^{-2}. Even in the *hybrid* models the production of Ne VIII is through collisional ionization.

5. The O V and O VI absorptions are consistent with a multi-phase origin, with contributions from both the $T \sim 10^4$ K photoionized gas traced by the H I, C III, O III, and O IV and the $T \sim 5 \times 10^5$ K collisionally ionized gas phase where the Ne VIII is produced. The metallicity for the collisionally ionized gas phase is consistent with the $-0.62 \leqslant [Z/H] \leqslant -0.15$ metallicity range estimated by Howk et al. (2009) for the photoionized gas phase in this absorber.

6. The Chen & Mulchaey (2009) imaging survey of the PKS 0405−123 field has identified a galaxy with rest-frame R magnitude of $M_R - 5 \log h_{70} = -19.6$ ($L \sim 0.08L_R^*$) at a projected separation of $\rho = 110h_{70}^{-1}$ kpc and at a systemic velocity of $\Delta v = -180$ km s^{-1} from the Ne VIII absorber.

7. The proximity of the absorber to the galaxy and their modest velocity displacement from each other suggests the possibility of the Ne VIII absorption arising in multiphase gas embedded in the *hot* halo of the galaxy. The physical properties and metallicity of the absorber are also consistent with an origin in a nearby intergalactic WHIM structure.

REFERENCES

Asplund, M., Grevesse, N., Sauval, A. J., & Scott, P. 2009, ARA&A, 47, 481
Bahcall, J. N., Jannuzi, B. T., Schneider, D. P., & Hartig, G. F. 1993, ApJ, 405, 491
Bregman, J. N. 2007, ARA&A, 45, 221
Cen, R., & Fang, T. 2006, ApJ, 650, 573
Cen, R., & Ostriker, J. P. 1999, ApJ, 514, 1
Cen, R., & Ostriker, J. P. 2006, ApJ, 650, 560
Chen, H.-W., & Mulchaey, J. S. 2009, ApJ, 701, 1219
Dahlen, T., Mobasher, B., Somerville, R. S., Moustakas, L. A., Dickinson, M., Ferguson, H. C., & Giavalisco, M. 2005, ApJ, 631, 126
Danforth, C. W., Keeney, B. A., Stocke, J. T., Shull, J. M., & Yao, Y. 2010, ApJ, 720, 976

Danforth, C. W., & Shull, J. M. 2008, ApJ, 679, 194
Danforth, C. W., Shull, J. M., Rosenberg, J. L., & Stocke, J. T. 2006, ApJ, 640, 716
Danforth, C. W., Stocke, J. T., & Shull, J. M. 2010, ApJ, 710, 613
Davé, R., et al. 2001, ApJ, 552, 473
Dixon, W. V., et al. 2010, Cosmic Origins Spectrograph Instrument Handbook, Version 2.0 (Baltimore, MD: STScI)
Ferland, G. J., Korista, K. T., Verner, D. A., Ferguson, J. W., Kingdon, J. B., & Verner, E. M. 1998, PASP, 110, 761
Fitzpatrick, E. L., & Spitzer, L., Jr. 1997, ApJ, 475, 623
Fox, A. J., Wakker, B. P., Savage, B. D., Tripp, T. M., Sembach, K. R., & Bland-Hawthorn, J. 2005, ApJ, 630, 332
Froning, C. S., & Green, J. C. 2009, Ap&SS, 320, 181
Fukugita, M., Hogan, C. J., & Peebles, P. J. E. 1998, ApJ, 503, 518
Fukugita, M., & Peebles, P. J. E. 2004, ApJ, 616, 643
Ghavamian, et al. 2009, Preliminary Characterization of the Post-Launch Line Spread Function of COS, http://www.stsci.edu/hst/cos/documents/isrs/
Gnat, O., & Sternberg, A. 2007, ApJS, 168, 213
Green, J. C. 2001, Proc. SPIE, 4498, 229
Haardt, F., & Madau, P. 2001, in Clusters of Galaxies and the High Redshift Universe Observed in X-rays, ed. D. M. Neumann & J. T. T. Van (Saclay: CEA)
Howk, J. C., Ribaudo, J. S., Lehner, N., Prochaska, J. X., & Chen, H.-W. 2009, MNRAS, 396, 1875
Jannuzi, B. T., et al. 1998, ApJS, 118, 1
Kim, T.-S., Hu, E. M., Cowie, L. L., & Songaila, A. 1997, AJ, 114, 1
Lehner, N., Prochaska, J. X., Kobulnicky, H. A., Cooksey, K. L., Howk, J. C., Williger, G. M., & Cales, S. L. 2009, ApJ, 694, 734
Lehner, N., Savage, B. D., Richter, P., Sembach, K. R., Tripp, T. M., & Wakker, B. P. 2007, ApJ, 658, 680
Lehner, N., Savage, B. D., Wakker, B. P., Sembach, K. R., & Tripp, T. M. 2006, ApJS, 164, 1
Lockman, F. J., & Savage, B. D. 1995, ApJS, 97, 1
Mulchaey, J. S., & Chen, H.-W. 2009, ApJ, 698, L46
Narayanan, A., Savage, B. D., & Wakker, B. P. 2010, ApJ, 712, 1443
Narayanan, A., Wakker, B. P., & Savage, B. D. 2009, ApJ, 703, 74
Narayanan, A., Wakker, B. P., Savage, B. D., Keeney, B. A., Shull, J. M., Stocke, J. T., & Sembach, K. R. 2010, ApJ, 721, 960

Oppenheimer, B. D., & Davé, R. 2009, MNRAS, 395, 1875
Osterman, S., et al. 2010, Astrophysics and Space Science, submitted (arXiv:1012.5827)
Penton, S. V., Shull, J. M., & Stocke, J. T. 2000, ApJ, 544, 150
Penton, S. V., Stocke, J. T., & Shull, J. M. 2004, ApJS, 152, 29
Prochaska, J. X., Chen, H.-W., Howk, J. C., Weiner, B. J., & Mulchaey, J. 2004, ApJ, 617, 718
Prochaska, J. X., & Tumlinson, J. 2009, in Astrophysics in the Next Decade (Astrophysics & Space Science Proceedings), ed. H. A. Thronson, M. Stiavelli, & A. G. G. M. Tielens (Dordrecht: Springer), 419
Richter, P., Savage, B. D., Sembach, K. R., & Tripp, T. M. 2006, A&A, 445, 827
Savage, B. D., Lehner, N., Wakker, B. P., Sembach, K. R., & Tripp, T. M. 2005, ApJ, 626, 776
Savage, B. D., & Sembach, K. R. 1991, ApJ, 379, 245
Savage, B. D., Sembach, K. R., Tripp, T. M., & Richter, P. 2002, ApJ, 564, 631
Savage, B. D., et al. 2010, ApJ, 719, 1526
Sembach, K. R., Tripp, T. M., Savage, B. D., & Richter, P. 2004, ApJS, 155, 351
Stocke, J. T., Penton, S. V., Danforth, C. W., Shull, J. M., Tumlinson, J., & McLin, K. M. 2006, ApJ, 641, 217
Thom, C., & Chen, H.-W. 2008a, ApJ, 683, 22
Thom, C., & Chen, H.-W. 2008b, ApJS, 179, 37
Tripp, T. M., Aracil, B., Bowen, D. V., & Jenkins, E. B. 2006, ApJ, 643, L77
Tripp, T. M., & Savage, B. D. 2000, ApJ, 542, 42
Tripp, T. M., Savage, B. D., & Jenkins, E. B. 2000, ApJ, 534, L1
Tripp, T. M., Sembach, K. R., Bowen, D. V., Savage, B. D., Jenkins, E. B., Lehner, N., & Richter, P. 2008, ApJS, 177, 39
Tumlinson, J., & Fang, T. 2005, ApJ, 623, L97
Tumlinson, J., Shull, J. M., Giroux, M. L., & Stocke, J. T. 2005, ApJ, 620, 95
Valageas, P., Schaeffer, R., & Silk, J. 2002, A&A, 388, 741
Verner, D. A., Barthel, P. D., & Tytler, D. 1994, A&AS, 108, 287
Wakker, B. P., & Savage, B. D. 2009, ApJS, 182, 378
Weymann, R. J., et al. 1998, ApJ, 506, 1
Williger, G. M., Heap, S. R., Weymann, R. J., Davé, R., Ellingson, E., Carswell, R. F., Tripp, T. M., & Jenkins, E. B. 2006, ApJ, 636, 631
Wright, E. L. 2006, PASP, 118, 1711